Eur. Phys. J. C (2025) 85:321
https://doi.org/10.1140/epjc/s10052-025-13917-4

THE EUROPEAN PHYSICAL JOURNAL C

Regular Article - Theoretical Physics

Constraining mass–radius limit of gravitationally decoupled binary compact star mergers PSR J0952-0607 and GW200210 generated by dual matter density profiles

S. K. Maurya[1,a], **M. K. Jasim**[1,b], **Abdelghani Errehymy**[2,3,c], **Phongpichit Channuie**[4,5,d], **G. Mustafa**[6,7,e], **Orhan Donmez**[8,f]

[1] Department of Mathematical and Physical Sciences, College of Arts and Sciences, University of Nizwa, P.O. Box 33, 616 Nizwa, Sultanate of Oman
[2] Astrophysics Research Centre, School of Mathematics, Statistics and Computer Science, University of KwaZulu-Natal, Private Bag X54001, Durban 4000, South Africa
[3] Center for Theoretical Physics, Khazar University, 41 Mehseti Str., Baku AZ1096, Azerbaijan
[4] School of Science, Walailak University, Nakhon Si Thammarat 80160, Thailand
[5] College of Graduate Studies, Walailak University, Nakhon Si Thammarat 80160, Thailand
[6] Department of Physics, Zhejiang Normal University, Jinhua 321004, People's Republic of China
[7] Research Center of Astrophysics and Cosmology, Khazar University, 41 Mehseti Street, AZ1096 Baku, Azerbaijan
[8] College of Engineering and Technology, American University of the Middle East, 54200 Egaila, Kuwait

Received: 22 October 2024 / Accepted: 9 February 2025

Abstract In this article, we present exact solutions to Einstein's field equations through a process known as minimally gravitational decoupling (MGD). Our study posits strange quark matter (SQM) as the initial seed source and introduces pseudo-Isothermal (PI) dark matter (DM) as the new source. We derive the metric potentials, deformation functions, and physical quantities of gravitating compact objects, thoroughly analyzing the MGD effect on these quantities. By applying Herrera's cracking concept and the adiabatic condition, we demonstrate that the anisotropic stellar system we studied, influenced by two interconnected sources, achieves stable equilibrium. Focusing on models related to the mass gap identified in the GW200210 event ($2.83^{+0.47}_{-0.42}$) and the "black widow" pulsar PSR J0952-0607 ($2.35^{+0.17}_{-0.17}$), the fastest known spinning neutron star in the Milky Way, we constrain the mass–radius relationship and moment of inertia values under the MGD effects within the framework of general relativity (GR). Our findings indicate that the maximum allowable mass tends to increase in the lower mass gap region as the MGD effect parameter β and the central DM density σ_1 rise. Conversely, this maximum mass decreases with an increase in the bag constant $\mathcal{B}_g$, which correlates with the surface density of SQM in our model. Interestingly, when the stellar structure undergoes deformation due to MGD, it responds differently to the density profiles of DM and SQM. Specifically, as $\mathcal{B}g$ increases, SQM tends to inhibit the formation of supermassive compact stars (CSs) governed by MGD and PI-DM. Notably, supermassive CSs can exceed 2 $M\odot$ for values of $\mathcal{B}_g \leq 62.5$ MeV fm^{-3}. Finally, we conclude that a maximum mass of approximately 3 $M_\odot$ in the mass gap region can be attained by incorporating DM and adjusting the MGD effects within the stellar structure under GR. The elevated moment of inertia values suggests a stiffer equation of state (EOS) for the current anisotropic system.

Contents

[a] e-mail: sunil@unizwa.edu.om
[b] e-mail: mahmoodkhalid@unizwa.edu.om
[c] e-mail: abdelghani.errehymy@gmail.com
[d] e-mail: phongpichit.ch@mail.wu.ac.th (corresponding author)
[e] e-mail: gmustafa3828@gmail.com
[f] e-mail: orhan.donmez@aum.edu.kw

Published online: 20 March 2025

1 Introduction

In the wake of the first confirmed observation of gravitational waves (GWs) from a binary black hole merger [1], a new period in the field of astrophysics has begun. Subsequently, another breakthrough in the detection of GW170817 and Gamma-ray burst (GRB 170817A) from the merger of a binary neutron star (NS) by LIGO and Virgo detectors [2] has profound impact on the study of astrophysics and cosmology [3]. In this connection, a recent study [4] claimed that the generation of GW echo from GW170817 can be associated with the features of strange stars (SSs) and consequently SS could be the source of GW echo. Hence, the EOS of quark matter has the possibility to be explored in the light of observed GWs generated from SS [5]. Particularly, values of strange quark mass and bag constant are constrained with the confirmed observation of f and lowest ω_{II} mode in GW events. Therefore, it would be interesting to investigate the characteristics and features of SS leading to keen implications for astrophysics and cosmology in the new era of GW astronomy.

SS is composed of SQM which comprises deconfined up, down, and strange quarks. It is remarkable to note that SQM is considered to be the absolute ground state of matter [6–10] according to the SQM hypothesis. In this regard, EOS of strange matter inside the SS is proposed by MIT bag model [11] which consists of a bag constant. In particular, the bag is referred to the color confinement of the quarks. Physically, one can obtain energy density by adding the bag constant to the kinetic energy of quarks [12]. Again, the quark pressure reduces due to enhancement in the value of the bag constant. Since the value of the bag constant is important in the configuration of an SS, the MIT bag model first proposed the standard value to be ≈ 55 MeV fm^{-3}. Later, a range of bag constants have been suggested in various studies [11,13,14]. Over the past three decades, different researchers have examined the features of SSs [15–23] due to its profound importance in strong interaction between physics and astrophysics.

Some studies suggest [24,25] that the DM and the stable nugget of SQM can be associated to each other where DM has become an enigmatic issue intriguing the scientific community for the past few years. This keeps various researchers from solving the puzzle of DM by proposing different models that basically represent axions, axion-like particles, and fermions as the most probable candidates of DM. Further, it has been suggested that self-interacting DM can exist in stellar configurations such as compact stars (CSs). In particular, research works [26,27] investigated different properties of boson stars where the bosonic DM particles have been considered with self-interaction. Other investigations [28,29] have taken self-interacting fermionic DM particles as constituents of a CS into account to explore the various features of CSs. In this connection, a recent study [30] indicates that the masses as well as the interaction strength of the DM particles along with the accumulation of cosmological structures play a crucial role in favor of the construction of CSs composed of self-interacting DM particles. Eventually, different features of astrophysical objects such as NSs, SSs, and white dwarfs (WDs) are significantly influenced by the occurrence of DM in stellar structures. As a consequence, in their quest for DM, researchers [31–33] are inclined to treat CSs as significant tools that are essentially useful to explore, analyze as well as constrain the characteristic features of DM. In this regard, mass–radius relation is considered to be one of the important aspects of CSs which can be influenced by the composition of stellar matter. The presence of DM in addition to normal matter or SQM in CSs can effectively show an impact on the mass–radius relations with respect to observational constraints. For instance, a research work [34] showed that the considerations of DM interactions can influence the physical features of quark stars.

In literature, there are various meticulous studies [35–40] which comprehensively examined and analyzed the impact of the presence of DM (Bosonic or Fermionic) on the properties and the compact structures of NSs considering the fact that the DM may or may not be self-interacting. In this field of study, researches indicated that exotic compact objects (COs) such as dark compact planets [41] could possibly exist. Further, GW sensors would be such well-equipped and competent currently and in the foreseeable future that it could probe and analyze the possible existence of DM [42–44] in NS mergers by adapting self-interaction strength and mass of the DM particle in the process of GW events. Moreover, with the advancement of GW astronomy, GW events from CO mergers can be detected in the not-too-distant future. Subsequently, the physical features of exotic COs that are made of DM can be examined and analyzed to unveil the mysteries about DM [45–47]. As a result, the detection techniques in

GW astronomy eventually will bring new prospects in the field of astrophysics like distinguishing the exotic objects from other CSs such as NS and BH on the basis of measuring differences in the observational aspects of COs [48].

In general, the dynamics of fluid-like configurations such as CSs are governed by the non-linear field equations in any gravity theory. A well-behaved non-singular and exact solution to the field equations which satisfies the necessary physical conditions represent a stable stellar structure. Among several techniques to solve the field equations, gravitational decoupling or geometrical decoupling (GD) emerges as an efficient method [49–62] to develop physically valid stellar models with a seed solution in addition to a new source. This effective technique can be utilized in two different ways which are (i) minimally gravitational decoupling (MGD) and (ii) complete gravitational decoupling (CGD) on the basis of physical requirements. As compared to the process of MGD, there is an exchange of energy between the seed source and the new source in CGD.

The presence of anisotropy in spherical fluid systems, i.e., COs was first investigated by Ruderman [63] in the background of GR. Subsequently, various researchers employed the anisotropy feature in their studies [64–66]. In particular, Bowers and Liang [65] have studied the impact of anisotropy in the relativistic COs following one of Bondi's earlier works which utilized the pressure anisotropy aspect to the isotropic system without assuming an EOS. The important result of their work was that the surface redshift and maximum allowable mass of the spherical fluid have larger values due to the anisotropic nature of the stellar system. The anisotropy arises due to different values of radial pressure and tangential pressure everywhere inside the system except at the center of the star. This can happen due to the presence of superconducting states, pion condensation [67,68], highly dense core, 3 A superfluidity, a mixture of different fluids, neutrino transport [69], the relativistic particles with high energy, etc. With this regard, various features of anisotropic radiating stars have been examined by Herrera and Santos [70].

It is worth noting that one of the stability criteria, namely adiabatic condition for isotropic systems as given by Chandrasekhar [71] is modified in the case of anisotropic systems in both Newtonian and post-Newtonian approximations. Herrera has shown in a recent work [72] that an isotropic relativistic fluid system always has a tendency to attain anisotropy whenever it undergoes a physical process. Again, Pretel [73] emphasized on the role of EOS which eventually measures the internal structure of the COs and constrains stability criteria accordingly. This fact is significant with regard to the GW170817 observation where bounds on the EOS for neutron-rich fluid as obtained by the LIGO-Virgo team [73,74]. Later on, measurement of tidal deformability of NS [75–84] advocate in behalf of the essential constraints on the EOS for nuclear densities in GW170817 event. In this connection, the recent detection of GW events indicating the occurrence of supermassive COs with masses greater than 2 $M_{\odot}$ is extremely relevant for constraining EOS in the study of compact star modeling. GW190814 [85] and GW200210 [86] are two such GW events each of which have a CO of mass 2.50–2.67 $M_{\odot}$ and $2.83^{+0.47}_{-0.42}$ $M_{\odot}$ respectively. These supermassive COs happen to fall in the lower end of the mass gap region which is considered as $M \approx [2.5, 5]$ $M_{\odot}$ [87], i.e., the mass gap between the heaviest NS and lightest BH.

Although the GD method is applied to the field equations governing the gravitating bodies with a motivation to introduce a new source via energy–momentum tensor, it has the additional benefit of incorporating anisotropy in the gravitating bodies successfully. In general, the seed system which may be or may not be isotropic in nature can behave as an anisotropic effective system through a mechanism of associating with the new anisotropic source. In this process, the seed solution in addition to anisotropic source counterparts to the field equations obtained by MGD or CGD, can represent a physical spherical fluid system that can be related to the observational constraints of observed COs. Further, the decoupling constant in the GD technique has a significant impact on the physical properties, mass–radius relations, stability conditions, and maximum mass limit of COs [88–90].

In a recent work [91], anisotropic CSs have been studied under the GD technique in the framework of GR where Einstein's Field Equations (EFE) are solved assuming null complexity factor condition [92] and generalized Durgapal–Fuloria metric ansatz [93] to determine the deformation functions [94]. This study favors all the physical features that represent Durgapal–Fuloria type superdense anisotropic CSs. In another work, Maurya et al. [95] have considered Pseudo Isothermal (PI) DM density profile [96,97] with zero complexity to perturb metric potentials in the process of CGD in the framework of GR where the seed system assumed to be a perfect fluid described in Vlasenko–Pronin space-time [98]. So, they have developed an anisotropic dark star model where the impact of decoupling constant on the effective system and GW echoes under CGD have been analyzed thoroughly. Based on the above theoretical discussions on the developments in the study of SQM, DM, and GD, we are motivated to study gravitationally deformed SQM systems by the process of MGD with the introduction PI-DM as a new source. Instead of considering the null complexity factor condition and a metric potential ansatz, we utilize the density profile given by Mak and Harko [120] for the seed system and the PI-DM density profile for the new system. Hence, we want to study the effective system governed by dual matter density profiles and relate the outcomes of the present study to the observational constraints of astrophysical COs.

The plan of the paper is arranged as follows: In Sect. 2 we have provided gravitationally decoupled EFEs which include

effective energy–momentum tensors representing the two sources of SQM and PI-DM. The decoupling process is utilized to obtain solutions to two sets of field equations for the seed system and new source in Sect. 3 by assuming the MIT bag EOS along with the density profile of SQM and PI-DM density profile. In Sect. 4, we have presented and utilized the boundary conditions to present the system. Further, the physical features of the solutions are analyzed in Sect. 5. The stability analysis under the cracking criterion and adiabatic condition have been shown in Sect. 6. Moreover, MGD effects on mass–radius relation and moment of inertia have been examined in Sects. 7 and 8 respectively. At last, final comments with brief discussion are given in Sect. 9.

2 Gravitationally decoupled Einstein field equation (EFE) generated by two sources

2.1 Field equations for gravitationally decoupled system

This section offers a concise summary of the gravitationally decoupled EFE for two distinct sources, with relativistic units expressed as $G = c = 1$,

$$G_{ij} = R_{ij} - \frac{1}{2}\, g_{ij}\, R = -8\pi \mathcal{C}_{ij}^{\text{eff}} \tag{1}$$

with,

$$\mathcal{C}_{ij}^{\text{eff}} = \mathcal{A}_{ij} + \beta\, \mathcal{H}_{ij}. \tag{2}$$

The expression R_{ij} is used to represent the Ricci tensor, where R stands for the contracted Ricci scalars and β serves as the coupling constant for the field equations. The energy–momentum tensor is represented as $\mathcal{A}_{ij}$, and additional fields, such as scalar, vector, and tensor fields, may be defined by the source $\mathcal{H}_{ij}$. Preserving the effective energy–momentum tensor $\mathcal{C}_{ij}^{\text{eff}}$ is necessary because the Einstein tensor (G_{ij}) fulfils the Bianchi identity,

$$\nabla_i [\mathcal{C}^{ij}]^{\text{eff}} = 0. \tag{3}$$

For the purpose of describing the space-time within the star system, a specific static spherically symmetric line element is being used:

$$ds^2 = -e^{\mathcal{K}_0(r)} dr^2 - r^2\left(d\theta^2 + \sin^2\theta\, d\phi^2\right) + e^{\mathcal{X}_0(r)} dt^2. \tag{4}$$

The metric potentials $\mathcal{X}_0$ and $\mathcal{K}_0$ are merely determined by radial distance. Considering that the internal configuration of the self-gravitating structure, described by the effective EMT $\mathcal{C}_{ij}^{\text{eff}}$, represents an anisotropic matter distribution,

$$\mathcal{C}_{ij}^{\text{eff}} = \left(\rho^{\text{eff}} + P_t^{\text{eff}}\right)\mathcal{U}_i\mathcal{U}_j - P_t^{\text{eff}} g_{ij} + (P_r^{\text{eff}} - P_t^{\text{eff}})\mathcal{V}_i\,\mathcal{V}_j. \tag{5}$$

The expression for u^i is articulated as: $u^i = e^{\mathcal{X}_0(r)/2}\delta^i{}_4$, consequently representing the four-velocity. The definition of $\chi^i = e^{\mathcal{K}_0(r)/2}\delta^i{}_1$ indicates that the unit vector in the radial direction is represented by the symbol χ^i. As ρ^{eff} describes the energy density of matter, P_r^{eff} represents the pressures in the radial direction and P_t^{eff} represents the pressures in the tangential direction. Moreover, the unit space-like vector u^i and the 4-velocity χ^i in the radial direction met the following requirements:

The comprehensive formulation of EFE can be articulated as a set of differential equations corresponding to the metric (1),

$$P_r^{\text{eff}} = \frac{1}{8\pi}\left[-\frac{1}{r^2} + e^{-\mathcal{K}_0}\left(\frac{1}{r^2} + \frac{\mathcal{X}_0'}{r}\right)\right] =, \tag{6}$$

$$P_t^{\text{eff}} = \frac{1}{8\pi}\left[\frac{e^{-\mathcal{K}_0}}{4}\left(2\mathcal{X}_0'' + \mathcal{X}_0'^2 - \mathcal{K}_0'\mathcal{X}_0' + 2\frac{\mathcal{X}_0' - \mathcal{K}_0'}{r}\right)\right], \tag{7}$$

$$\rho^{\text{eff}} = \frac{1}{8\pi}\left[\frac{1}{r^2} - e^{-\mathcal{K}_0}\left(\frac{1}{r^2} - \frac{\mathcal{K}_0'}{r}\right)\right]. \tag{8}$$

The use of the metric function facilitates the calculation of the mass function, $m(r)$, of a anisotropic fluid sphere,

$$e^{-\mathcal{K}_0} = 1 - \frac{2m(r)}{r}. \tag{9}$$

It is also equivalent to

$$m(r) = \frac{8\pi}{2}\int \rho^{\text{eff}}\, r^2 dr. \tag{10}$$

However, the pressure gradient can additionally be expressed as a function of $\mathcal{X}_0$, ρ^{eff}, P_r^{eff}, and P_t^{eff} via Eqs. (6)–(8),

$$\frac{dP_r^{\text{eff}}}{dr} = -\frac{\mathcal{X}_0'}{2}(P_r^{\text{eff}} + \rho^{\text{eff}}) + \frac{2(P_t^{\text{eff}} - P_r^{\text{eff}})}{r}. \tag{11}$$

The generalized hydrostatic Tolman–Oppenheimer–Volkoff equation for anisotropic celestial structure is presented in Eq. (11) [117,118].

3 Gravitationally decoupling approach via MGD and its solution using dual density matter profiles

Our subsequent objective is to ascertain an exact solution for the field equations (6)–(8) that characterize the structure of a SS. When we look at the system of field equations, we can see that it is not linear at all, which makes it hard to solve. This is why we use a different technique known as gravitational decoupling, which makes use of the minimal geometric deformation (MGD) approach via a particular transformation connected to the gravitational potential [121],

$$\mathcal{X}_0(r) \longrightarrow \mathcal{Y}_0(r) + \beta\, \mathcal{D}_g(r), \tag{12}$$

$$e^{-\mathcal{K}_0(r)} \longrightarrow \mathcal{W}_0(r) + \beta\, \mathcal{D}_h(r). \tag{13}$$

Let $\mathcal{D}_g(r)$ and $\mathcal{D}_h(r)$ denote the decoupling functions associated with the temporal and radial metric components, respectively. The deformation may be precisely calibrated by modifying the decoupling constant β. When $\beta = 0$, the standard theory of GR is completely reinstated. Utilising the MGD approach, we can ascertain that $\mathcal{D}_g(r) = 0$ and $\mathcal{D}_h(r) \neq 0$. This discovery indicates that the suitable transformation pertains only to the radial part of the metric function, whereas the temporal component stays unchanged. This MGD approach divides the decoupled system (6)–(8) into two separate components. The primary system is linked to $\mathcal{A}_{ij}$, whereas the secondary system pertains to the supplementary source $\mathcal{H}_{ij}$. To establish the starting system, we analyze the energy–momentum tensor $\mathcal{A}_{ij}$ that defines an anisotropic matter distribution represented by,

$$\mathcal{A}_{ij} = (\rho + P_t)\,\mathcal{U}_i\,\mathcal{U}_j - P_t\,\delta_{ij} + (P_r - P_t)\,\mathcal{V}_i\,\mathcal{V}_j. \tag{14}$$

Specifically, ρ represents the energy density while p_r and p_t, respectively, represent the radial and tangential pressures for the seed solution. Consequently, the effective amounts may be articulated as follows:

$$\rho^{\text{eff}} = \rho + \beta\,\mathcal{H}_0^0, \quad P_r^{\text{eff}} = P_r - \beta\,\mathcal{H}_1^1, \quad P_t^{\text{eff}} = P_t - \beta\,\mathcal{H}_2^2. \tag{15}$$

Furthermore, the related effective anisotropy is,

$$\Delta^{\text{eff}} = P_t^{\text{eff}} - P_r^{\text{eff}} = \Delta_{GR} + \Delta_\theta, \quad \text{where,} \quad \Delta_{GR} = P_t - P_r \quad \text{and} \quad \Delta_\theta = \beta(\mathcal{H}_1^1 - \mathcal{H}_2^2). \tag{16}$$

The two anisotropies associated with the matter distribution, $\mathcal{A}_{ij}$ and $\mathcal{H}_{ij}$, may be combined to define the effective anisotropy. The anisotropy (Δ_θ) is produced by gravitational decoupling and has the potential to augment the effective anisotropy. Assuming that the force arising from the anisotropic features of the fluid is represented by the expression $\frac{2(P_t^{\text{eff}} - P_r^{\text{eff}})}{r}$. The force is directed outward when the pressure P_t^{eff} is greater than the pressure P_r^{eff}. The force exerted is inwardly acting when P_t^{eff} is smaller than P_r^{eff}. However, if the value of P_t^{eff} exceeds that of P_r^{eff}, the force facilitates the development of a more compact structure in the context of an anisotropic fluid compared to an isotropic fluid distribution [119].

By using the transformations (12) and (13), the system (6)–(8) may be divided into two systems. In particular, when $\beta = 0$, the initial system depends on the gravitational potentials $\mathcal{Y}_0$ and $\mathcal{W}_0$,

$$\rho = \frac{1}{8\pi}\left(\frac{1}{r^2} - \frac{\mathcal{W}_0}{r^2} - \frac{\mathcal{W}_0'}{r}\right), \tag{17}$$

$$P_r = \frac{1}{8\pi}\left(-\frac{1}{r^2} + \frac{\mathcal{W}_0}{r^2} + \frac{\mathcal{Y}_0'\mathcal{W}_0}{r}\right), \tag{18}$$

$$P_t = \frac{1}{8\pi}\left(\frac{\mathcal{W}_0'\mathcal{Y}_0'}{4} + \frac{\mathcal{Y}_0''\mathcal{W}_0}{2} + \frac{\mathcal{Y}_0'^2\mathcal{W}_0}{4} + \frac{\mathcal{W}_0'}{2r} + \frac{\mathcal{Y}_0'\mathcal{W}_0}{2r}\right), \tag{19}$$

Eq. (8) yields the following outcome:

$$-\frac{\mathcal{Y}_0'}{2}(\rho + P_r) - P_r' + \frac{2}{r}(P_t - P_r) = 0. \tag{20}$$

The configuration of the system is represented by the TOV equation (17)–(19), whose solution may be found in the spacetime that is shown below,

$$ds^2 = e^{\mathcal{Y}_0(r)}dt^2 - \frac{dr^2}{\mathcal{W}_0(r)} - r^2 d\theta^2 + r^2\sin^2\theta\, d\phi^2. \tag{21}$$

By turning on β, we can deduce the subsequent set of equations as follows:

$$\mathcal{H}_0^0 = -\frac{1}{8\pi}\left(\frac{\mathcal{D}_h}{r^2} + \frac{\mathcal{D}_h'}{r}\right), \tag{22}$$

$$\mathcal{H}_1^1 = -\frac{1}{8\pi}\left(\frac{\mathcal{D}_h}{r^2} + \frac{\mathcal{Y}_0'\mathcal{D}_h}{r}\right), \tag{23}$$

$$\mathcal{H}_2^2 = -\frac{1}{8\pi}\left(\frac{1}{4}\mathcal{D}_h'\mathcal{Y}_0' + \frac{1}{2}\mathcal{Y}_0''\mathcal{D}_h + \frac{1}{4}\mathcal{Y}_0'^2\mathcal{D}_h + \frac{\mathcal{D}_h'}{2r} + \frac{\mathcal{Y}_0'\mathcal{D}_h}{2r}\right). \tag{24}$$

The subsequent link is established using the linear combination of Eqs. (22)–(24) as follows:

$$-\frac{\mathcal{Y}_0'}{2}(\mathcal{H}_0^0 - \mathcal{H}_1^1) + (\mathcal{H}_1^1)' + \frac{2}{r}(\mathcal{H}_1^1 - \mathcal{H}_2^2) = 0. \tag{25}$$

The following formula may be used to represent the mass distribution for each system as,

$$m_{GR} = \frac{1}{2}\int_0^r \rho(x)\,x^2 dx \text{ and } m_{\mathcal{D}} = \frac{1}{2}\int_0^r \mathcal{H}_0^0(x)\,x^2 dx. \tag{26}$$

The mass functions associated with sources $\mathcal{A}_{ij}$ and $\mathcal{H}_{ij}$ are represented by the symbols $m_{GR}(r)$ and $m_{\mathcal{D}}(r)$, correspondingly. Next, we will go over how to use the two matter density profiles in DM holes to determine the solutions to each set of differential equations separately.

3.1 Seed solution of the field equations (17)–(19) for source $\mathcal{A}_{ij}$ for SS models

To analyze the SS model, we assume that the distribution of SQM among the unusual stars is governed by the fundamental physical MIT bag model EOS. The implementation of the unique bag function in the bag model has maintained all modifications to the energy and pressure functions of the SQM methodology. Our basic bag model posits that the quarks are non-interacting and devoid of mass. The quark pressure will

be specified as,

$$P_r = \sum_{f=u,\ d,\ s} P^f - \mathcal{B}_g. \tag{27}$$

Let P^f denote the distinct pressures corresponding to the quark flavours (u), (d), and (s). The total external Bag pressure, or Bag constant $\mathcal{B}_g$, neutralizes these pressures. The amount of energy (ρ) associated with deconfined quarks within the context of the MIT Bag model may be articulated as follows:

$$\rho = \sum_f \rho^f + \mathcal{B}_g, \quad \text{where } \rho^f = 3P^f. \tag{28}$$

Utilizing Eqs. (27) and (28), in conjunction with the relation $\rho^f = 3P^f$, we can define the MIT bag EOS for strange quark star entities in its precise formulation,

$$P_r = \frac{1}{3}(\rho - 4\mathcal{B}_g). \tag{29}$$

To achieve a non-singular, monotonically declining matter density inside the spherically symmetric stellar structure, we elect a modified form of ρ as suggested by Mak and Harko [120],

$$\rho(r) = \rho_0\left[1 - \left(1 - \frac{\rho_s}{\rho_0}\right)\frac{r^2}{R^2}\right]. \tag{30}$$

The constants ρ_0 and ρ_s denote the highest and lowest amounts of ρ at the center and surface, respectively. Realistic matter density and realistic EoS have now been established with clarity. We now concentrate on the spacetime geometries $\mathcal{Y}_0$ and $\mathcal{W}_0$ pertaining to the initial system. The differential equation obtained from Eqs. (17) and (30) can be described in the following manner:

$$r\mathcal{W}_0'(r) + \mathcal{W}_0(r) + \frac{r^4(\rho_s - \rho_0) + r^2\rho_0 R^2 - 8\pi R^2}{8\pi R^2} = 0. \tag{31}$$

Upon completing the process of integration, we determine the potential $\mathcal{W}_0$,

$$\mathcal{W}_0 = \frac{8\pi r^2\rho_0(3r^2 - 5R^2) - 24\pi r^4\rho_s + 15R^2}{15R^2}. \tag{32}$$

To determine the alternative potential, we integrate the EOS (29) with Eq. (18), resulting in the following differential equation,

$$3\mathcal{W}_0 r\mathcal{Y}_0' - [8\pi\rho r^2 - 32\pi\mathcal{B}_g r^2 - 3\mathcal{W}_0 + 3] = 0. \tag{33}$$

When integrating above Eq. (33), the value of $\mathcal{Y}_0(r)$ may be found as follows:

$$\begin{aligned}\mathcal{Y}_0(r) = {} & \frac{2\sqrt{10\pi}R(\rho_0 - 6\mathcal{B}_g)}{3\sqrt{10\pi\rho_0^2R^2 - 9\rho_0 + 9\rho_s}} \\ & \times \tanh^{-1}\left[\frac{\sqrt{\frac{2\pi}{5}}\left(-6\rho_0 r^2 + 5\rho_0 R^2 + 6\rho_s r^2\right)}{R\sqrt{10\pi\rho_0^2R^2 - 9\rho_0 + 9\rho_s}}\right] \\ & -\frac{2}{3}\ln\left(8\pi\rho_0 r^2\left(3r^2 - 5R^2\right) - 24\pi\rho_s r^4 + 15R^2\right) \\ & + \mathcal{F}.\end{aligned} \tag{34}$$

The Eqs. (32) and (33) establish the comprehensive spacetime structure for the initial solution. Nonetheless, considering the $\mathcal{H}_{ij}$-sector, It is important to determine the results of the subsequent Eqs. (22)–(24). This second system has been solved previously using the well-known techniques $\rho = \mathcal{H}_0^0$ and $p_r = \mathcal{H}_1^1$ proposed by Ovalle [121–123]. Inspired by those studies, we apply the mimic technique in our current work to solve the system of equations (22)–(24). But it mimic approach will be done in the context of DM density profile rather than the well-known techniques $\rho = \mathcal{H}_0^0$ and $p_r = \mathcal{H}_1^1$ proposed by Ovalle [121]. The next section focuses the procedure for determining the deformation function using the DM density profile.

3.2 Solution of extra source $\mathcal{H}_{ij}$ using the DM density profile

Our current objective is to build the Dark Star models through gravitational decoupling. In light of the current conditions, we focus on the $\mathcal{H}_{ij}$-sector by modelling the ρ^θ-component via a PI-DM density profile [124,125], expressed as,

$$\rho_d = \frac{\sigma_1}{1 + \sigma_2\, r^2}. \tag{35}$$

Additionally, the research findings on DM halos and galaxy rotation curves are provided in the following publications [124,125], especially for certain parameter values denoted by σ_1 and σ_2. In our present investigation, we have treated constants as an independent variable. The density profile ρ_d exhibits regularity when there are no singularities. Moreover, the function of r demonstrates a consistently decreasing tendency throughout every finite area.

Utilising a mimicking strategy by aligning $8\pi\mathcal{H}_0^0$ with ρ_d, we construct the subsequent differential equation in $\mathcal{D}_h(r)$ as follows:

$$\frac{d\mathcal{D}_h}{dr} + \frac{\mathcal{D}_h}{r} = -\frac{\sigma_1}{1 + \sigma_2\, r^2}. \tag{36}$$

Upon doing the integration procedure, we get the resultant equation for $\mathcal{D}_h(r)$ as

$$\mathcal{D}_h(r)=\frac{8\pi\,\sigma_1\,\tan^{-1}\left(\sqrt{\sigma_2}\,r\right)}{\sigma_2^{3/2}r}-\frac{8\pi\,\sigma_1}{\sigma_2}+\frac{\mathcal{K}_1}{r}. \tag{37}$$

From the deformed metric function $e^{-\mathcal{K}_0(r)}=\mathcal{W}_0(r)+\beta\mathcal{D}_h$, it can be inferred that the deformation function $\mathcal{D}_h$ must disappear at the centre. To fulfil the specified requirement, the arbitrary constant $\mathcal{K}_1$ must be eliminated. Finally, the deformation function is,

$$\mathcal{D}_h(r)=\frac{8\pi\,\sigma_1\,\tan^{-1}\left(\sqrt{\sigma_2}\,r\right)}{\sigma_2^{3/2}r}-\frac{8\pi\,\sigma_1}{\sigma_2}. \tag{38}$$

The formulae for the source $\mathcal{H}_{ij}$ are provided as follows:

$$\mathcal{H}_0^0=\frac{\sigma_1}{r^2\sigma_2+1}, \tag{39}$$

$$\begin{aligned}\mathcal{H}_1^1=&-\frac{1}{r^3\sigma_2^{3/2}\left(8\pi\rho_0r^2\left(3r^2-5R^2\right)-24\pi\rho_sr^4+15R^2\right)}\\&\times\Big[5\sigma_1\left(r\sqrt{\sigma_2}-\tan^{-1}\left(r\sqrt{\sigma_2}\right)\right)\left(R^2\left(32\pi\mathcal{B}_gr^2-3\right)\\&+8\pi\rho_0r^2\left(r^2-R^2\right)-8\pi\rho_sr^4\right)\Big],\end{aligned} \tag{40}$$

$$\begin{aligned}\mathcal{H}_2^2=&-\frac{\sigma_1}{2r^3\sigma_2^{3/2}\left(r^2\sigma_2+1\right)\mathcal{H}_{22}(r)}\Big[\Big(r^2\sigma_2\tan^{-1}\left(r\sqrt{\sigma_2}\right)\\&-r\sqrt{\sigma_2}+\tan^{-1}\left(r\sqrt{\sigma_2}\right)\Big)\Big(8\pi\rho_0r^2\left(3r^2-5R^2\right)\\&-24\pi\rho_sr^4+15R^2\Big)\Big[5R^2\left(16\pi\mathcal{B}_gr^2-3\right)+8\pi\rho_0r^4\\&-8\pi\rho_sr^4\Big]-32\pi r^2\left(r^2\sigma_2+1\right)\left(r\sqrt{\sigma_2}-\tan^{-1}\left(r\sqrt{\sigma_2}\right)\right)\\&\times\Big\{5\rho_0R^2\Big(112\pi\mathcal{B}_gr^4-8r^2\left(10\pi\mathcal{B}_gR^2+3\right)+15R^2\Big)\\&+40\rho_sr^2R^2\left(3-14\pi\mathcal{B}_gr^2\right)+50\mathcal{B}_gR^4\left(8\pi\mathcal{B}_gr^2-3\right)\\&+4\pi\rho_0^2r^2\left(16r^4-30r^2R^2+25R^4\right)-8\pi\rho_0\rho_sr^4\\&\times\left(16r^2-15R^2\right)+64\pi\rho_s^2r^6\Big\}\Big],\end{aligned} \tag{41}$$

where, $\mathcal{H}_{22}(r)=\left(8\pi\rho_0r^2\left(3r^2-5R^2\right)-24\pi\rho_sr^4+15R^2\right)^2$ The newly deformed solution may be expressed by the following line element, and the gravitational potential is provided by,

$$\begin{aligned}ds^2=&\left[\frac{8\pi r^2\rho_0(3r^2-5R^2)-24\pi r^4\rho_s+15R^2}{15R^2}-\frac{8\pi\,\sigma_1}{\sigma_2}\right.\\&\left.+\frac{8\pi\,\beta\,\sigma_1\,\tan^{-1}\left(\sqrt{\sigma_2}\,r\right)}{\sigma_2^{3/2}r}\right]^{-1}dr^2+e^{\mathcal{X}_0(r)}dt^2\\&-r^2\left(d\theta^2+\sin^2\theta\,d\phi^2\right),\end{aligned} \tag{42}$$

where,

$$\begin{aligned}e^{\mathcal{X}_0(r)}=&\frac{2\sqrt{10\pi}\,R(\rho_0-6\mathcal{B}_g)}{3\sqrt{10\pi\rho_0^2R^2-9\rho_0+9\rho_s}}\\&\times\tanh^{-1}\left[\frac{\sqrt{\frac{2\pi}{5}}\left(-6\rho_0r^2+5\rho_0R^2+6\rho_sr^2\right)}{R\sqrt{10\pi\rho_0^2R^2-9\rho_0+9\rho_s}}\right]\\&-\frac{2}{3}\ln\left[8\pi\rho_0r^2\left(3r^2-5R^2\right)-24\pi\rho_sr^4+15R^2\right]+\mathcal{F}.\end{aligned} \tag{43}$$

The effective system expressions, using the aforementioned line element, assume the following form.

$$\rho^{\text{eff}}=\frac{\beta\sigma_1+\left(r^2\sigma_2+1\right)\left(r^2(\rho_s-\rho_0)+\rho_0R^2\right)}{R^2\left(r^2\sigma_2+1\right)}, \tag{44}$$

$$\begin{aligned}P_r^{\text{eff}}=&\frac{1}{3r^3R^2\sigma_2^{3/2}\left(8\pi\rho_0r^2\left(3r^2-5R^2\right)-24\pi\rho_sr^4+15R^2\right)}\\&\times\Big[-15\beta R^2\sigma_1\left(r\sqrt{\sigma_2}-\tan^{-1}\left(r\sqrt{\sigma_2}\right)\right)\left(R^2(3\right.\\&-32\pi\mathcal{B}_gr^2)+8\pi\rho_0r^2\left(R^2-r^2\right)+8\pi\rho_sr^4\Big)-r^3\sigma_2^{3/2}\\&\times\left(-24\pi\rho_0r^4+40\pi\rho_0r^2R^2+24\pi\rho_sr^4-15R^2\right)\\&\times\left(-4\mathcal{B}_gR^2+\rho_0\left(R^2-r^2\right)+\rho_sr^2\right)\Big],\end{aligned} \tag{45}$$

$$\begin{aligned}P_t^{\text{eff}}=&\frac{P_{t1}(r)}{2r^3\sigma_2^{3/2}\left(r^2\sigma_2+1\right)P_{t2}(r)}-\frac{1}{P_{t3}(r)}\Big[\rho_0R^2\Big(128\pi\mathcal{B}_gr^4\\&-10r^2\left(8\pi\mathcal{B}_gR^2+3\right)+15R^2\Big)+2\rho_sr^2R^2(15\\&-64\pi\mathcal{B}_gr^2)+20\mathcal{B}_gR^4\left(8\pi\mathcal{B}_gr^2-3\right)+8\pi\rho_0^2r^2\\&\times\left(2r^4-5r^2R^2+5R^4\right)-8\pi\rho_0\rho_sr^4\left(4r^2-5R^2\right)\\&+16\pi\rho_s^2r^6\Big].\end{aligned} \tag{46}$$

4 Boundary conditions for SS models under gravitational decoupling

To create a plausible compact stellar model, defined by a restricted and finite matter distribution with a specific mass M and radius R, it is crucial to link the internal geometry $\mathcal{M}^-$ at the surface $\Sigma=r=R$ with the external space-time $\mathcal{M}^+$ that envelops the structure. Within the framework of the GR system, the external manifolds are mostly identified as Schwarzschild vacuum space-time, particularly in the case of uncharged, non-radiating, and static compact objects. It is essential to analyse the attributes of the supplementary component of the energy–momentum tensor, namely the $\mathcal{H}_{ij}$-sector. This new expression may change the material content of the external space-time. The exact geometry defining this

outer manifold may be expressed as,

$$ds^2 = \left[1 - \frac{2\mathcal{M}}{r}\right] dt^2 - \frac{dr^2}{1 - \frac{2\mathcal{M}}{r}} - r^2 d\Omega^2. \tag{47}$$

To effectively connect the internal structure with the exterior one, the ID junction circumstances require to make use of both the first and second fundamental forms. The first fundamental form establishes the continuity of the metric potentials at the σ boundary. The first fundamental form is outlined below:

$$e^{\mathcal{Y}_0^-(r)}|_{r=R} = e^{\mathcal{Y}_0^+(r)}|_{r=R}, \tag{48}$$

and

$$e^{-\mathcal{X}_0^-(r)}|_{r=R} = e^{-\mathcal{X}_0^+(r)}|_{r=R}. \tag{49}$$

In this context, the symbols "−" and "+" denote the inner and outer structures, respectively. The second fundamental form relates to the continuity of the extrinsic curvature $K_{\mu\nu}$ induced by the components $\mathcal{M}^-$ and $\mathcal{M}^+$ on the surface of the object. The continuity of the K_{rr} component across the boundary results in

$$\left[P_r^{(\text{eff})}(r)\right]_{r=R} = \left[P_r^{(\text{eff})}(r) - \beta\,\theta_r^1(1)\right]_{r=R} = 0. \tag{50}$$

Utilizing the aforementioned condition, we establish the quantity of the bag constant as,

$$\begin{aligned}\mathcal{B}_g = &\Big[\rho_s R^3 \sigma_2^{3/2}\left(16\pi\rho_0 R^2 + 24\pi\rho_s R^2 - 15\right) + 15\beta\sigma_1 \\ &\times\left(8\pi\rho_s R^2 + 3\right)\left(R\sqrt{\sigma_2} - \tan^{-1}\left(R\sqrt{\sigma_2}\right)\right)\Big]\Big/\Big[4R^2 \\ &\times\Big(R\sigma_2^{3/2}\left(16\pi\rho_0 R^2 + 24\pi\rho_s R^2 - 15\right) - 120\pi\beta\sigma_1 \\ &\times\left(\tan^{-1}\left(R\sqrt{\sigma_2}\right) - R\sqrt{\sigma_2}\right)\Big)\Big].\end{aligned} \tag{51}$$

5 Physical analysis of density, pressure and anisotropy

The physical quantities such as density (ρ^{eff}), the effective pressure both in radial (P_r^{eff}) and tangential (P_t^{eff}) directions, and the anisotropy (Δ^{eff}) will be analysed in this section to investigate the physical acceptance of the present stellar model including dual matter densities for SQM and PI-DM decoupled via MGD in the framework of GR. The variation of the physical quantities with respect to radial distance for different values of β have been shown graphically in Fig. 1 which indicates the solution to the field equations is well behaved and non singular throughout the stellar configuration.

One of the necessary requirements for a physical system which is satisfied in the present model as shown in Fig. 1 is that all the physical quantities must be finite and non negative inside the star. It is to be noted that density and pressure are maximum at centers and decreases monotonically for increasing radial distance towards the surface of the star. The effect of dual matter density along with MGD in the effective stellar system maintains the vanishing condition of radial pressure which eventually identifies the boundary of the star. The numerical values of density at center and surface, central pressure have been provided in Table 1. It can be seen that the values of the central density and surface density are the order of 10^{14} g cm^{-3} whereas the values of central pressure are the order of 10^{34} dyne cm^{-2} obtained within the physically acceptable range for different values of β.

An essential feature of an anisotropic stellar model is the equality of radial pressure and tangential pressure to be hold at the center of the system. This feature well established in the present model as anisotropy panel in Fig. 1 shows that the values of P_r^{eff} and P_t^{eff} do not differ at the center for various values of β or the MGD effect. Since anisotropy of the system is measured as the difference in values of P_r^{eff} and P_t^{eff}, central anisotropy of the system remains zero for increasing values of β. As one approaches towards the surface of the star from the center, the difference of P_r^{eff} and P_t^{eff} becomes positive and grows monotonically. Hence, anisotropy increases throughout the star and reaches its maximum value at the boundary of the star. The positive Δ^{eff} plays a significant role to stabilize the system as it appears to be the repulsive anisotropic force which acts opposite to the attractive gravitational force to offer a stable equilibrium to the stellar system.

6 Stability analysis

6.1 Stability for stellar COs using cracking criterion

First of all, we have investigated whether the causality is maintained in the present stellar model. For this we have presented graphically the variation of square of the sound speeds in both radial and tangential directions with respect to radial distance in Fig. 2 which ensures that both the sound speeds (v_r^2 and v_t^2) are less than the speed of sound or unity for all increasing values of β. Apparently, the MGD effects in GR do not violate causality.

Another aspect of studying variation of sound speeds inside the star is to evaluate the equilibrium status of the present system which may be stable or unstable configurations subject to cracking concept given by Herrera [112]. This criteria identifies the stable and unstable regions in the stellar system depending on the following conditions

$$\begin{aligned}&-1 \le v_t^2 - v_r^2 \le 1 \\ &= \left\{\begin{array}{ll} -1 \le v_t^2 - v_r^2 \le 0 & \text{Potentially stable} \\ 0 < v_t^2 - v_r^2 \le 1 & \text{Potentially unstable}\end{array}\right\}.\end{aligned} \tag{52}$$

In Fig. 3 we have shown the variation of the difference between the v_r^2 and v_t^2 with respect to radial distance for

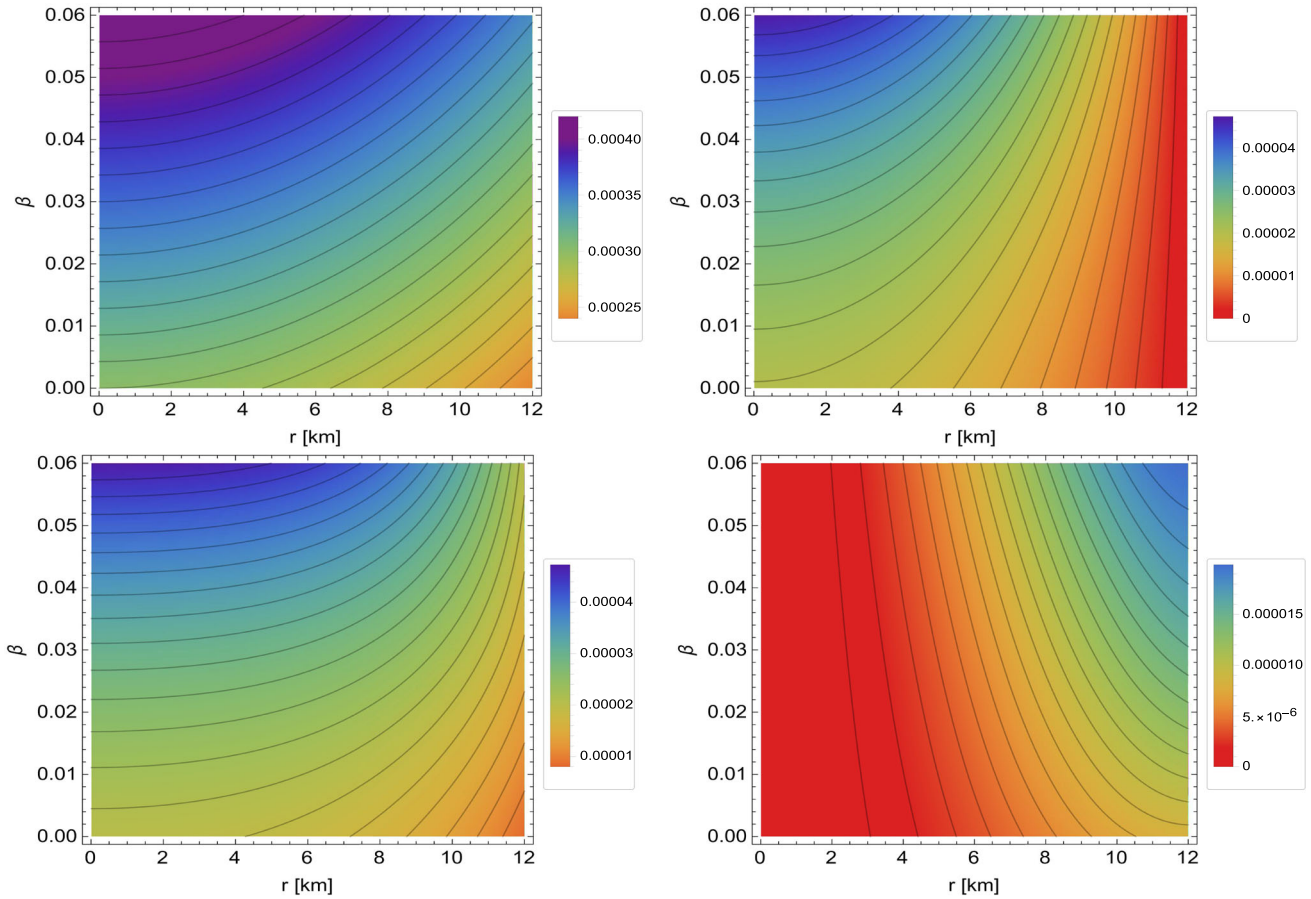

Fig. 1 Nature of effective density (ρ^{eff}-top left panel), radial pressure (P_r^{eff}-top right panel), tangential pressure (P_t^{eff}-bottom left panel), and anisotropy (Δ^{eff}-bottom right panel) against radial coordinate r with $\rho_0 = 0.0003$ km^{-2}, $\rho_s = 0.00024$ km^{-2}, $\sigma_1 = 0.002$ km^{-2}, and $\sigma_2 = 0.001$ km^{-2} for different values of β

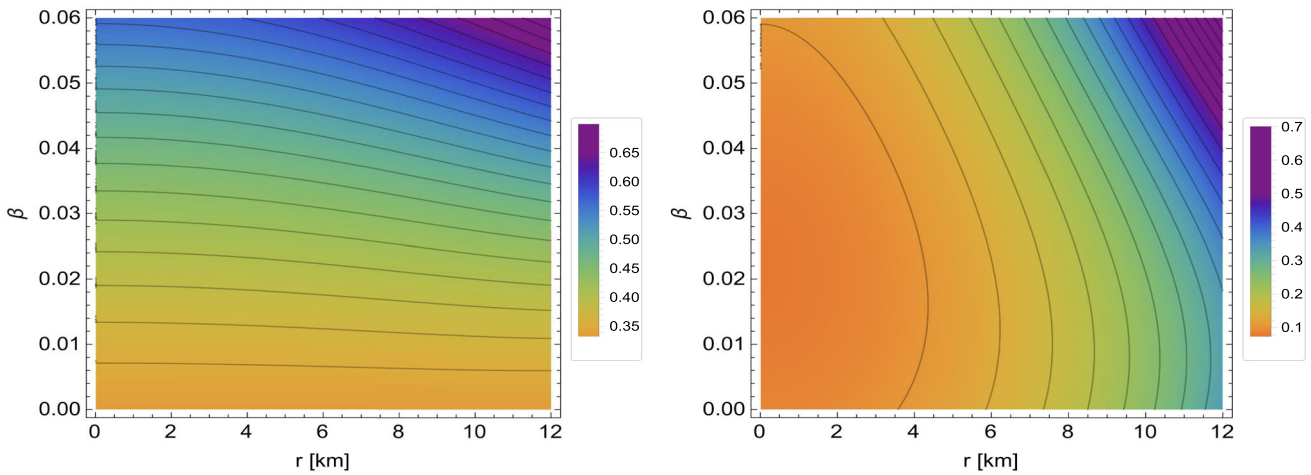

Fig. 2 Nature of radial velocity (v_r^2-left panel) and tangential velocity (v_t^2-right panel) against radial coordinate r with $\rho_0 = 0.0003$ km^{-2}, $\rho_s = 0.00024$ km^{-2}, $\sigma_1 = 0.002$ km^{-2}, and $\sigma_2 = 0.001$ km^{-2} for different values of β

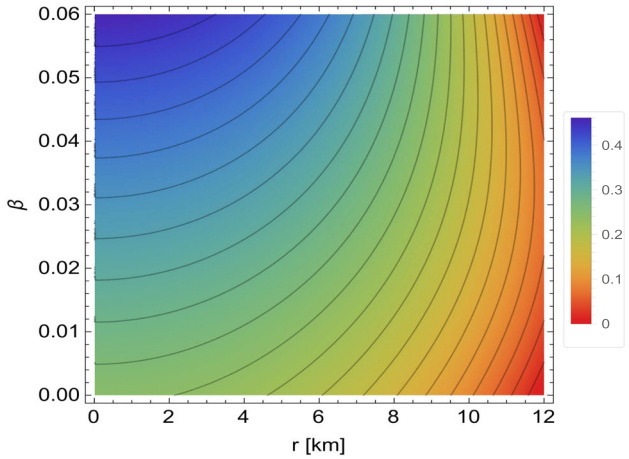

Fig. 3 Nature of stability factor $(v_r^2 - v_t^2)$ against radial coordinate r with $\rho_0 = 0.0003$ km^{-2}, $\rho_s = 0.00024$ km^{-2}, $\sigma_1 = 0.002$ km^{-2}, and $\sigma_2 = 0.001$ km^{-2} for different values of β

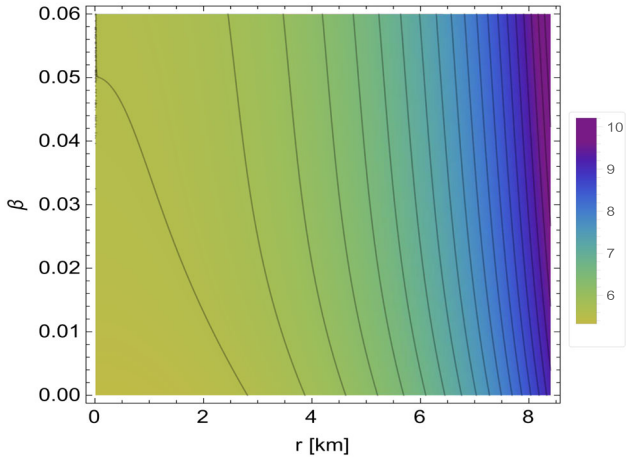

Fig. 4 Nature of adiabatic index (Γ) against radial coordinate r with $\rho_0 = 0.0003$ km^{-2}, $\rho_s = 0.00024$ km^{-2}, $\sigma_1 = 0.002$ km^{-2}, and $\sigma_2 = 0.001$ km^{-2} for different values of β

increasing β to determine stable regions in the star. It can be seen from Fig. 3 that the whole region inside the star satisfies condition for stable equilibrium for $0 \leq \beta \leq 0.06$. Interestingly, values of β larger than 0.06 lead the effective system to fall in status of unstable equilibrium. This confirms that MGD has a significant role to stabilize the system with some constrained values of β. So, the value of β can not be arbitrarily large on account of the stability of the effective system. In the state of stable equilibrium the v_r^2 remains greater than the v_t^2 in the stellar system. So, with presence of dual matter density connected via MGD, the sound speeds satisfy Herrera's inequality in the stellar system to achieve stable equilibrium.

6.2 Adiabatic condition for stability

There is another way to determine the stability of a stellar configurations that is known as adiabatic condition. This condition [113,114] states that the adiabatic index defined as

$$\Gamma = \left(1 + \frac{\rho^{\text{eff}}}{P_r^{\text{eff}}}\right)\left(\frac{dP_r^{\text{eff}}}{d\rho^{\text{eff}}}\right) \tag{53}$$

can not be smaller than 4/3 in case of stable equilibrium of an isotropic stellar configuration. On the other hand, the revised stability condition [115,116] for an anisotropic stellar configurations is given by

$$\Gamma > \frac{4}{3} + \left[\frac{4}{3}\frac{(P_t^{\text{eff}} - P_r^{\text{eff}})}{|(P_r^{\text{eff}})'|r}\right]. \tag{54}$$

Since the present stellar model is anisotropic in nature with presence of dual matter, we have shown variation of Γ with respect to radial distance for increasing β in Fig. 4. Interestingly, Γ is non-negative finite throughout the star for increasing β. It is always much larger than 4/3 at the center of the star and has an increasing nature with respect to radial distance to reach its maximum values at the surface of the star. The central values of Γ which are greater than 5.33 have been listed in Table 1. So, the present model with MGD effect continue to be in stable equilibrium under the adiabatic condition in background of GR.

7 Impact of dual density profiles on the mass–radius relations

In the present work, assuming density profiles for SQM as well as for PI-DM with anisotropy, stellar configurations for anisotropic CSs are developed in the framework of GR. With regard to mass gap region we have considered observed stars like PSR J1614-2230 [99] and PSR J0952-0607 [100], GW190814 [85] and GW200210 [86] as SS candidates to evaluate the limit of maximum mass of NSs. So, we have correlated the observed masses of the stars to the mass–radius curves drawn with respect to varying model parameters in the present study. In particular, the $M-R$ curves for different values of β representing the effect of MGD and σ_1 implying the influence PI-DM have been shown in the left and right panels of the Fig. 5 respectively. Again the $M-R$ curves with respect to bag constant $\mathcal{B}_g$ indicating the impact of SQM is shown in the left panel of Fig. 7.

Each peak of the $M-R$ curves depicts the maximum mass (M_{max}) which can have larger values towards the lower mass gap region for increasing β, σ_1 and decreasing $\mathcal{B}_g$. The corresponding radius to each peak is also increased with the same effect of the parameters. It is interesting to note that M_{max} increases with increasing effect of MGD and the central density for DM but decreases with increasing bag constant which is related to surface density for SQM in the present model. When the SS is deformed with MGD, the effective system

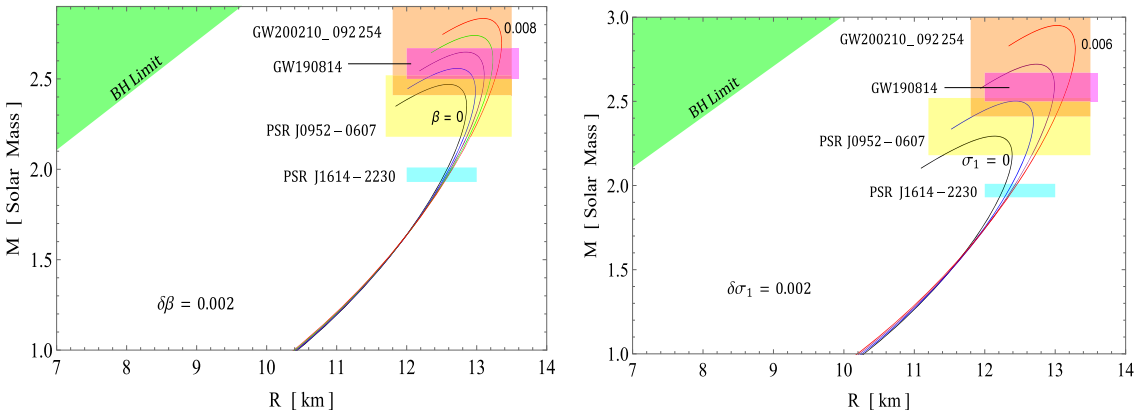

Fig. 5 $M-R$ curves for different values of β and σ_1 for $\rho_0 = 0.0003/\text{km}^2, \rho_s = 0.00024/\text{km}^2, \sigma_1 = 0.002/\text{km}^2, \sigma_2 = 0.001/\text{km}^2$ and $\rho_0 = 0.0003/\text{km}^2, \rho_s = 0.00024/\text{km}^2, \beta = 0.005, \sigma_2 = 0.001/\text{km}^2$

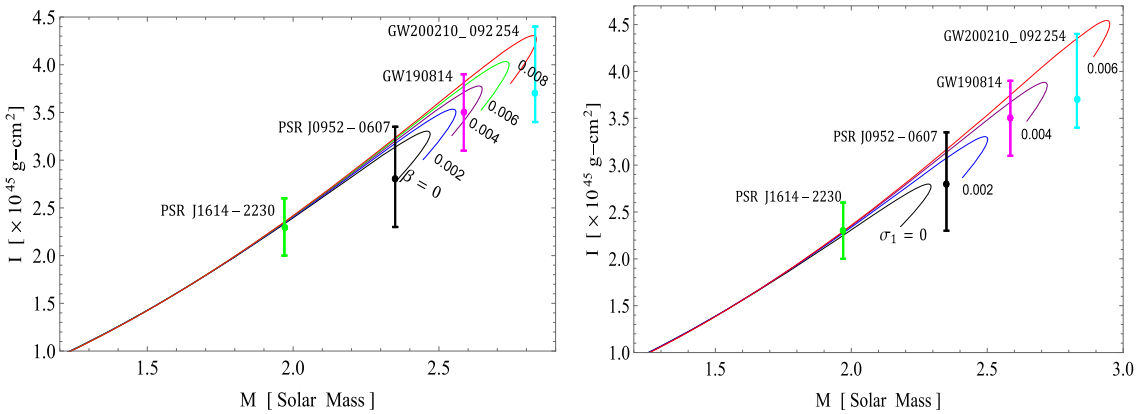

Fig. 6 $M-R$ curves for different values of β and σ_1 for $\rho_0 = 0.0003/\text{km}^2, \rho_s = 0.00024/\text{km}^2, \sigma_1 = 0.002/\text{km}^2, \sigma_2 = 0.001/\text{km}^2$ and $\rho_0 = 0.0003/\text{km}^2, \rho_s = 0.00024/\text{km}^2, \beta = 0.005, \sigma_2 = 0.001/\text{km}^2$

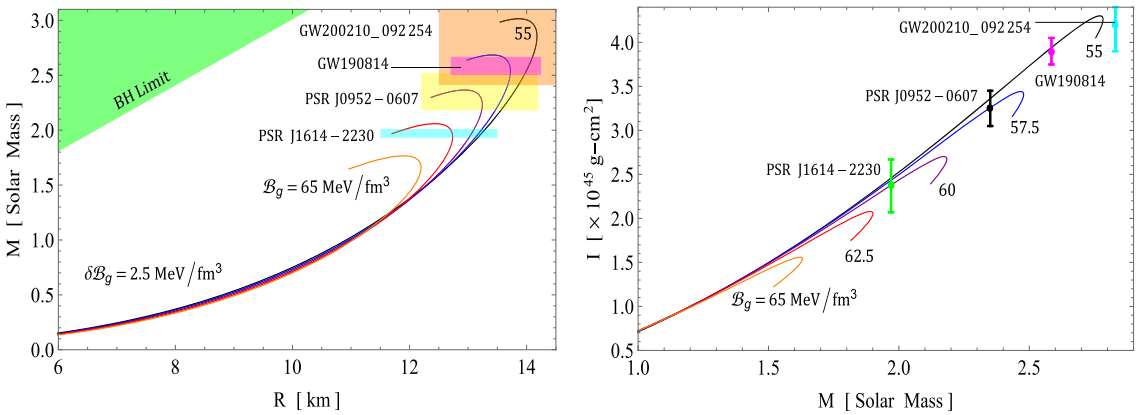

Fig. 7 $M-R$ curves for different values of $\mathcal{B}_g$ for $\rho_0 = 0.000277/\text{km}^2, \rho_s = 0.00024/\text{km}^2, \sigma_2 = 0.001/\text{km}^2$

Table 1 The numerical values of the physical parameters in respect to decoupling parameter β

Parameters	P_{r0}^{eff} (dyne/cm^2)	ρ_0^{eff} (gm/cm^3)	ρ_s^{eff} (gm/cm^3)	Γ
$\beta = 0.00$	2.42983×10^{34}	4.04888×10^{14}	3.23911×10^{14}	5.33334
$\beta = 0.02$	3.15339×10^{34}	4.58874×10^{14}	3.71101×10^{14}	5.48944
$\beta = 0.04$	4.22869×10^{36}	5.12859×10^{14}	4.1829×10^{14}	5.57613
$\beta = 0.06$	5.74134×10^{36}	5.66844×10^{14}	4.6548×10^{14}	5.68951

responds to two density profiles for DM and SQM in a contrary manner to each other. In particular, with increasing $\mathcal{B}_g$, SQM acts in such a way in the present dual matter effective system that it has inclination towards opposing the development of supermassive CSs governed by MGD and PI-DM. Notably, the supermassive CSs can have a mass larger than 2 $M_\odot$ for the values $\mathcal{B}_g \leq 62.5$ MeV fm^{-3}. Hence, we can infer that $M_{max} \approx 3\ M_\odot$ in the mass gap region can be achieved by incorporating DM content and tuning the MGD effect in the SS with the background of GR.

The nature of variation of the $M-R$ curves in Figs. 5 and 7 shows a quark matter type EOS with respect to the variation in the parameters. This is in concurrence with the MIT bag EOS that we have assumed in the seed system. So, the effective system behaves like the seed system from the perspective of mass–radius relation but shows constraints on measurements of M_{max} and radius due to the impact of MGD and DM. The fact that $M-R$ curves are found to be within the Buchdahl limit establishes the physical validity of the present model.

Different techniques involved in determining the radii of COs are apparently challenging to process in comparison with the measurements of the mass of COs [101,102] based on the observed parameters. However, at present, there are some new methods available to probe the radii of COs. For instance, one can determine the estimated radii of COs by examining hotspots of NSs as observed by NICER [103,104]. In particular, an investigation by NICER and XMM-Newton related to the patterns of hotspots of the rotating NSs led to the measurement of the estimated radius of PSR J0740+6620 to be $13.70^{+2.6}_{-1.5}$ km [105] with 68% credibility. Again, the determination of tidal deformability factor in connection to GW events [106] is another way to probe the radii of COs. In order to examine the influence of MGD, density profiles of SQM, and DM, the predicted radii from the present study have been tabulated in Tables 2 and 4 by considering the observed masses of the four SS candidates. The predicted radius of the secondary companion of GW190814 falls in the range of [12.99 km, 14.02 km] subject to variation of all the parameters.

8 Effect of dual density profiles on moment of inertia

Some studies suggested that the moment of inertia is an anticipated observational quantity to be determined with good accuracy [107,108] pertaining to the detection of double NSs in the near future. An empirical expression for the moment of inertia (I) formulated with total mass and radius for a static solution is given by Bejger and Haensel [109] in the form as

$$I = \frac{2}{9}\left(1 + \frac{5(M_{NR}/R_{NR})\text{km}}{M_\odot}\right) M_{NR} R_{NR}^2, \tag{55}$$

with a constraint given as

$$(M_{NR}/R_{NR})(\text{km}/M_\odot) > 0.1.$$

Here M_{NR} and R_{NR} are termed as the mass and radius of the non-rotating (NR) star respectively. This empirical formula is utilized to determine the moment of inertia of the present system and to examine its dependence on the total mass of the stellar system for variations in the parameters β, σ_1 and $\mathcal{B}_g$. The moment of inertia-total mass relation has been shown in the form of the $I-M$ curves with respect to parameters β and σ_1 in both panels of Fig. 6. Again, the $I-M$ curves with regard to the values of $\mathcal{B}_g$ have been shown in the right panel of Fig. 7.

Each maximum point of the $I-M$ curves refers to the maximum moment of inertia (I_{max}) which can have greater values for increasing β, σ_1 and decreasing $\mathcal{B}_g$. The corresponding total mass to each peak of $I-M$ curves is also enhanced with the same effect of the parameters. It is worth noting that I_{max} tends to get higher values with increasing effect of MGD and the DM central density parameter but decreases with increasing bag constant in the present model. Similar to the $M-R$ relation, the effective system responds to two density profiles for DM and SQM in the case of the $I-M$ relation. In order to investigate the impact of MGD, density profiles of SQM and DM, the predicted moment of inertia from the present model have been tabulated in Tables 3 and 4 for the four SS candidates.

One of the motivations for studying $M-R$ as well as $I-M$ relations is to assess the stiffness of an EOS. In this case, the $I-M$ curves seem to be more sensitive than the $M-R$ curves to measure the stiffness of the EOS precisely. For example, if the M_{max} of a star becomes twice the initial mass theoretically due to the transition of EOS towards a stiffer EOS, the I_{max} increases by seven times to initial values [111] for the same transition. In a work [63], the values of the moment of inertia were found to be in a broader range $[0.007,\ 0.7] \times 10^{45}$ g cm^2 because of the uncertainty present in the EOS at high densities. In case of supermassive SSs, we determined the range of values of I from Table 3 as $[2.33,\ 4.30] \times 10^{45}$ g cm^2 for $0 \leq \beta \leq 0.008$ and as $[2.25,\ 4.35] \times 10^{45}$ g cm^2 for $0 \leq \sigma_1 \leq 0.006$. Table 4 indicates the range of I to be $[2.37,\ 3.93] \times 10^{45}$ g cm^2 for 55 MeV fm$^{-3} \leq \mathcal{B}_g \leq 65$ MeV fm^{-3}. So, the present model presents higher values of the moment of inertia for the supermassive SSs. In this relation, we can mention a work [110] which considered various EOS like RP, FP, CDK, BJ, and TI with increasing stiffness and central density of the order of $10^{14} g/cm^3$ to show the values of I_{max} of the PSR 1937+21 falling in range of $[1.1,\ 2.4] \times 10^{45}$ g cm^2. Hence, we can infer that the stiffer EOS corresponds to higher values of I in a stellar model. In our model, the higher values of I indicate that the supermassive SSs are governed by stiffer EOS.

Table 2 The predicted radii of few high mass CSs corresponding Fig. 5

Objects	$\frac{M}{M_\odot}$	Predicted R (km)					Predicted R (km)			
		β					σ_1			
		0	0.002	0.004	0.006	0.008	0	0.002	0.004	0.006
PSR J1614-2230 [99]	1.97 ± 0.04	$12.53^{+0.06}_{-0.05}$	$12.56^{+0.06}_{-0.06}$	$12.58^{+0.06}_{-0.06}$	$12.59^{+0.06}_{-0.06}$	$12.61^{+0.05}_{-0.07}$	$12.25^{+0.04}_{-0.04}$	$12.33^{+0.06}_{-0.05}$	$12.38^{+0.06}_{-0.07}$	$12.40^{+0.06}_{-0.07}$
PSR J0952-0607 [100]	2.35 ± 0.17	$12.85^{-}_{-0.08}$	$12.96^{+0.01}_{-0.14}$	$13.03^{+0.07}_{-0.17}$	$13.08^{+0.13}_{-0.19}$	$13.12^{+0.15}_{-0.20}$	–	$12.69^{-}_{-0.11}$	$12.85^{+0.12}_{-0.18}$	$12.94^{+0.18}_{-0.23}$
GW190814 [85]	2.5–2.67	–	–	$13.09^{+0.01}_{-}$	$13.22^{+0.01}_{-0.02}$	$13.31^{+0.05}_{-0.05}$	–	–	$12.99^{+0.04}_{-0.03}$	$13.16^{+0.08}_{-0.06}$
GW200210 [86]	$2.83^{+0.47}_{-0.42}$	–	–	–	–	$13.17^{+0.02}_{-}$	–	–	–	$13.28^{-}_{-0.27}$

9 Concluding remarks

In the present analysis of the anisotropic CSs in the background of GR, we have examined the impact of MGD on the effective system in the presence of SQM and PI-DM. Firstly, we considered EFEs which include effective energy–momentum tensors representing the sources of SQM and PI-DM decoupled with MGD parameter β. The decoupling process is utilized to obtain two sets of field equations for the two sources present in the system. We have obtained a solution to the metric potentials for the seed system by assuming the MIT bag EOS along with the density profile of SQM. In MGD, the radial component of the spacetime metric is deformed by some new function that appears in the field equations for the new source. We got the solution for the deformation function by considering the PI-DM density profile. In most cases, MGD can be useful to introduce anisotropy to the perfect fluid solution. However, we have considered the MGD approach to investigate the impact on the anisotropy of the seed system for including the DM source. At last, we have analyzed the physical features of the solutions to EFEs and mass–radius relation with respect to parameters.

The nature of variation of the physical quantities such as ρ^{eff}, P_r^{eff}, P_t^{eff} and Δ^{eff} with respect to radial distance for different values of β shown graphically in Fig. 1 have confirmed that the solution to the EFEs is well behaved and non-singular throughout the stellar configuration. In this regard, all the physical quantities are finite and non-negative inside the star. Density and pressure having maximum values at centers are seen to decrease monotonically for increasing radial distance towards the surface of the star.

The effect of dual matter density along with MGD in the effective stellar system does not violate the vanishing condition of radial pressure in the present study. The numerical values of density at center and surface, central pressure provided in Table 1 are the order of 10^{14} g cm^{-3} and 10^{34} dyne cm^{-2} respectively for different values of β.

The vanishing of central anisotropy is well established in the present model under the MGD approach for various values of β which is shown in the anisotropy panel in Fig. 1. The anisotropy becomes positive and grows monotonically towards the surface of the star from the center. It reaches a maximum value at the boundary of the star for various values of β. The positive Δ^{eff} plays another significant role to stabilize the system as it appears to be the repulsive anisotropic force that counterbalances attractive gravitational force.

We have depicted that the causality is maintained in the present stellar model by showing the variation of the square of the sound speeds in both radial and tangential directions graphically in Fig. 2. This means that both the sound speeds are less than the speed of sound for different values of β. So, MGD effects in GR follow causality.

Table 3 The predicted radii of few high mass CSs corresponding Fig. 6

Objects	$\frac{M}{M_\odot}$	Predicted $I \times 10^{45}$ (g-cm^2)					Predicted $I \times 10^{45}$ (g-cm^2)			
		β					σ_1			
		0	0.002	0.004	0.006	0.008	0	0.002	0.004	0.006
PSR J1614-2230 [99]	1.97 ± 0.04	2.33	2.33	2.33	2.33	2.33	2.25	2.27	2.30	2.30
PSR J0952-0607 [100]	2.35 ± 0.17	3.13	3.17	3.23	3.22	3.24	–	3.07	3.13	3.17
GW190814 [85]	2.5−2.67	–	–	3.71	3.77	3.81	–	–	3.67	3.75
GW200210 [86]	$2.83^{+0.47}_{-0.42}$	–	–	–	–	4.30	–	–	–	4.35

Table 4 The predicted radii of few high mass CSs corresponding Fig. 7

Objects	$\frac{M}{M_\odot}$	Predicted radius				Predicted $I \times 10^{45}$ (g $\cdot$ cm^2)			
		$\mathcal{B}_g$				$\mathcal{B}_g$			
		55	57.5	60	62.5	55	57.5	60	62.5
PSR J1614-2230 [99]	1.97 ± 0.04	$13.24^{+0.06}_{-0.08}$	$13.19^{+0.04}_{-0.06}$	$13.06^{+0.04}_{-0.05}$	$12.72^{+0.02}_{-0.01}$	2.47	2.43	2.37	–
PSR J0952-0607 [100]	2.35 ± 0.17	$13.80^{+0.17}_{-0.24}$	$13.64^{+0.08}_{-0.18}$	$13.07^{+0.25}_{-}$	–	3.35	3.25	–	–
GW190814 [85]	$2.5 - 2.67$	$14.02^{+0.08}_{-0.07}$	$13.72^{+0.01}_{-0.10}$	–	–	3.93	–	–	–
GW200210 [86]	$2.83^{+0.47}_{-0.42}$	$14.17^{-}_{-0.03}$	–	–	–	–	–	–	–

In Fig. 3 the variation of the difference between the v_r^2 and v_t^2 with respect to radial distance for increasing β shows that the whole region inside the star satisfies Herrera's condition for stable equilibrium for $0 \leq \beta \leq 0.06$. Interestingly, the MGD effect constrains the higher values of β larger than 0.06 as the effective system becomes unstable. Therefore, the MGD effect along with the presence of dual matter density, the sound speeds satisfy Herrera's inequality in the stellar system to achieve stable equilibrium.

We have shown a variation of Γ with respect to radial distance for increasing β in Fig. 4 which indicates that Γ is non-negative and finite positive slope throughout the star for increasing β. It has much larger values than 4/3 at the center of the star as it can be seen from Table 1 where the central values of Γ greater than 5.33 have been listed. As a consequence, the present model with the MGD effect continues to be in stable equilibrium under the adiabatic condition in the background of GR.

In the present work, in connection to the mass gap region we have considered observed stars like PSR J1614-2230 [99] and PSR J0952-0607 [100], GW190814 [85] and GW200210 [86] as SS candidates and correlated the observed masses of the stars to the mass–radius curves drawn with respect to varying model parameters to examine the limit of maximum mass of NSs. The $M-R$ curves for different values of MGD parameter (β) and DM parameter (σ_1) have been shown in the left and right panels of the Fig. 5 respectively. Again the $M-R$ curves with respect to bag constant $\mathcal{B}_g$ indicating the impact of SQM have been shown in the left panel of Fig. 7. The nature of variation of the $M-R$ curves in Figs. 5 and 7 shows a quark matter type EOS with respect to the variation in the parameters. The fact that $M-R$ curves are found to be within the Buchdahl limit establishes the physical validity of the present model.

The peaks of the $M-R$ curves imply that the maximum mass (M_{max}) can have larger values towards the lower mass gap region with increasing effect of MGD and the central density for DM but decreases with increasing bag constant which is related to surface density for SQM in the present model. The corresponding radius to each peak is also increased with the same effect of the parameters. It is interesting to note that M_{max} increases When the SS is deformed with MGD but with increasing $\mathcal{B}_g$, SQM acts in such a way in the present dual matter effective system incline to oppose the development of supermassive CSs. Notably, MGD constrains the $\mathcal{B}_g$ to be greater than 62.5 MeV fm^{-3} in case of the supermassive CSs having mass larger than 2 $M_\odot$. Therefore, it can be inferred that $M_{max} \approx 3\ M_\odot$ in the mass gap region can be achieved by incorporating DM content and tuning the MGD effect in the SS with the background of GR. We have examined the influence of MGD, density profiles of SQM and DM by measuring the predicted radii which have been tabulated in Tables 2 and 4 by considering the observed masses of the four SS candidates in the present study. The predicted radius of the secondary companion of GW190814 falls in the range of [12.99 km, 14.02 km] subject to variation of all the parameters.

The $I-M$ relation has been shown with respect to parameters β and σ_1 in both panels of Fig. 6 and with regard to the values of $\mathcal{B}_g$ have been shown in the right panel of Fig. 7. It

is important to note that I_{max} tends to get higher values with increasing effect of MGD and the DM central density parameter but decreases with increasing bag constant in the present model. So, the effective system responds to the $I-M$ relation as similar to the $M-R$ relation for dual matter density. The predicted moment of inertia from the present model has been tabulated in Tables 3 and 4 for the four SS candidates. In case of supermassive SSs, we determined the range of values of I from Table 3 as $[2.33,\ 4.30]\times 10^{45}$ g cm^2 for $0 \leq \beta \leq 0.008$ and as $[2.25,\ 4.35]\times 10^{45}$ g cm^2 for $0 \leq \sigma_1 \leq 0.006$. Table 4 indicates the range of I to be $[2.37,\ 3.93]\times 10^{45}$ g cm^2 for 55 MeV fm$^{-3} \leq \mathcal{B}_g \leq 65$ MeV fm^{-3}. So, the present model presents higher values of the moment of inertia for the supermassive SSs. Hence, we can infer that the stiffer EOS corresponds to higher values of I in a stellar model in connection to a work [110] which considered various EOS like RP, FP, CDK, BJ, and TI with increasing stiffness and central density of the order of 10^{14} g/cm^3 to show the values of I_{max} of the PSR 1937+21 falling in range of $[1.1,\ 2.4]\times 10^{45}$ g cm^2. In our model, the higher values of I indicate that the supermassive SSs are governed by stiffer EOS.

As a final point, it is important to note that the present investigation explores the salient features of a well-behaved physical solution to the EFEs representing the impact of MGD on anisotropic and uncharged matter distribution with density profiles of SQM and DM. In the future, there is scope for studying MGD effects on anisotropic and charged stellar configurations with dual matter density profiles in the framework of GR and other modified theories of gravity.

Acknowledgements The authors SKM and MKJ are also thankful for continuous support and encouragement from the administration of the University of Nizwa for this research work. AE thanks the National Research Foundation of South Africa for the award of a postdoctoral fellowship.

Funding The author SKM and MKJ acknowledge that this research work is supported by the TRC Project (Grant No. BFP/RGP/CBS/24/203).

Data Availability Statement This manuscript has no associated data or the data will not be deposited. [Author's comment: There is no observational data related to this article. The necessary calculations and graphic discussion are already available in the manuscript.]

Code Availability Statement This manuscript has no associated code/software. [Author's comment: This is a theoretical work and no new code/software has been generated. The numerical computation has been performed using Mathematica and Python software.]

Declarations

Conflict of interest The authors declare no conflict of interest.

Funded by SCOAP[3].

Appendix

$$
\begin{aligned}
P_{t1}(r) = \beta\sigma_1\Big[& \left(r^2\sigma_2 \tan^{-1}\left(r\sqrt{\sigma_2}\right) - r\sqrt{\sigma_2} + \tan^{-1}\left(r\sqrt{\sigma_2}\right)\right) \\
& \times \left(8\pi\rho_0 r^2\left(3r^2 - 5R^2\right) - 24\pi\rho_s r^4 + 15R^2\right)\left(5R^2\right. \\
& \times \left(16\pi\mathcal{B}_g r^2 - 3\right) + 8\pi\rho_0 r^4 - 8\pi\rho_s r^4\Big) - 32\pi r^2\left(r^2\sigma_2 + 1\right) \\
& \times \left(r\sqrt{\sigma_2} - \tan^{-1}\left(r\sqrt{\sigma_2}\right)\right)\Big)\Big(5\rho_0 R^2(112\pi\mathcal{B}_g r^4 - 8r^2 \\
& \times \left(10\pi\mathcal{B}_g R^2 + 3\right) + 15R^2) + 40\rho_s r^2 R^2\left(3 - 14\pi\mathcal{B}_g r^2\right) \\
& + 50\mathcal{B}_g R^4\left(8\pi\mathcal{B}_g r^2 - 3\right) + 4\pi\rho_0^2 r^2\left(16r^4 - 30r^2R^2 + 25R^4\right) \\
& - 8\pi\rho_0\rho_s r^4\left(16r^2 - 15R^2\right) + 64\pi\rho_s^2 r^6\Big)\Big],
\end{aligned}
$$

$$
P_{t2}(r) = \left(8\pi\rho_0 r^2\left(3r^2 - 5R^2\right) - 24\pi\rho_s r^4 + 15R^2\right)^2,
$$

$$
P_{t3}(r) = 3R^2\left(-24\pi\rho_0 r^4 + 40\pi\rho_0 r^2 R^2 + 24\pi\rho_s r^4 - 15R^2\right).
$$

References

1. B.P. Abbott et al., Phys. Rev. Lett. **116**, 061102 (2016)
2. B.P. Abbott et al., Astrophys. J. Lett. **848**, L13 (2017)
3. B.P. Abbott et al., Phys. Rev. Lett. **119**, 161101 (2017)
4. M. Mannarelli, F. Tonelli, Phys. Rev. D **97**, 123010 (2018)
5. H. Sotani, K. Kohri, T. Harada, Phys. Rev. D **69**, 084008 (2004)
6. A.R. Bodmer, Phys. Rev. D **4**, 160 (1971)
7. E. Witten, Phys. Rev. D **30**, 272 (1984)
8. H. Terazawa, J. Phys. Soc. Jpn. **58**, 3555 (1989)
9. H. Terazawa, J. Phys. Soc. Jpn. **58**, 4388 (1989)
10. H. Terazawa, J. Phys. Soc. Jpn. **59**, 1199 (1990)
11. E. Farhi, R.L. Jaffe, Phys. Rev. D **30**, 2379 (1984)
12. G.H. Bordbar, H. Bahri, F. Kayanikhoo, Res. Astron. Astrophys. **12**, 1280 (2012)
13. N. Stergioulas, Living Rev. Relativ. **6**, 3 (2003)
14. A. Aziz, S. Ray, F. Rahaman, M. Khlopov, B.K. Guha, Int. J. Mod. Phys. D **28**, 1941006 (2019)
15. N. Itoh, Prog. Theor. Phys. **44**, 291 (1970)
16. C. Alcock, E. Farhi, A. Olinto, Astrophys. J. **310**, 261 (1986)
17. P. Haensel, J.L. Zdunik, R. Schaefer, Astron. Astrophys. **160**, 121 (1986)
18. C. Alcock, A. Olinto, Annu. Rev. Nucl. Part. Sci. **38**, 161 (1988)
19. J. Madsen, Physics and astrophysics of strange quark matter, in *Hadrons in Dense Matter and Hadrosynthesis. Lecture Notes in Physics*, vol. 516, ed. by J. Cleymans, H.B. Geyer, F.G. Scholtz (Springer, Berlin, 1999)
20. I. Bombaci, I. Parenti, I. Vidaña, Astrophys. J. **614**, 314 (2004)
21. F. Weber, Prog. Part. Nucl. Phys. **54**, 193 (2005)
22. J. Staff, R. Ouyed, M. Bagchi, Astrophys. J. **667**, 340 (2007)
23. M. Herzog, F.K. Röpke, Phys. Rev. D **84**, 083002 (2011)

24. A. Bhattacharyya, J.E. Alam, S. Sarkar, P. Roy, B. Sinha, S. Raha, P. Bhattacharjee, Nucl. Phys. A **661**, 629c (1999)
25. J.P. VanDevender, A.P. VanDevender, T. Sloan, C. Swaim, P. Wilson, R.G. Schmitt, N. McGinley, Sci. Rep. **7**, 8758 (2017)
26. M. Colpi, S.L. Shapiro, I. Wasserman, Phys. Rev. Lett. **57**, 2485 (1986)
27. J. Eby, C. Kouvaris, N.G. Nielsen, L.C.R. Wijewardhana, JHEP **02**, 028 (2016)
28. C. Kouvaris, N.G. Nielsen, Phys. Rev. D **92**, 063526 (2015)
29. M.I. Gresham, K.M. Zurek, Phys. Rev. D **99**, 083008 (2019)
30. J.H. Chang, D. Egana-Ugrinovic, R. Essig, C. Kouvaris, JCAP **03**, 036 (2019)
31. C. Kouvaris, P. Tinyakov, Phys. Rev. D **82**, 063531 (2010)
32. M. McCullough, M. Fairbairn, Phys. Rev. D **81**, 083520 (2010)
33. R. Garani, Y. Genolini, T. Hambye, JCAP **05**, 035 (2019)
34. P. Mukhopadhyay, J. Schaffner-Bielich, Phys. Rev. D **93**, 083009 (2016)
35. F. Sandin, P. Ciarcelluti, Astropart. Phys. **32**, 278 (2009)
36. A. Li, F. Huang, R.-X. Xu, Astropart. Phys. **37**, 70 (2012)
37. G. Baym, D.H. Beck, P. Geltenbort, J. Shelton, Phys. Rev. Lett. **121**, 061801 (2018)
38. D. McKeen, A.E. Nelson, S. Reddy, D. Zhou, Phys. Rev. Lett. **121**, 061802 (2018)
39. W. Husain, T.F. Motta, A.W. Thomas, JCAP **10**, 028 (2022)
40. M. Cassing, A. Brisebois, M. Azeem, J. Schaffner-Bielich, Astrophys. J. **944**, 130 (2023)
41. L. Tolos, J. Schaffner-Bielich, Y. Dengler, Phys. Rev. D **92**, 123002 (2015)
42. C.J. Horowitz, S. Reddy, Phys. Rev. Lett. **122**, 071102 (2019)
43. A. Nelson, S. Reddy, D. Zhou, JCAP **07**, 012 (2019)
44. D.R. Karkevandi, S. Shakeri, V. Sagun, O. Ivanytskyi, Phys. Rev. D **105**, 023001 (2022)
45. A. Maselli, S.H. Völkel, K.D. Kokkotas, Phys. Rev. D **96**, 064045 (2017)
46. Z. Mark, A. Zimmerman, S.M. Du, Y. Chen, Phys. Rev. D **96**, 084002 (2017)
47. S. Wystub, Y. Dengler, J.-E. Christian, J. Schaffner-Bielich, Mon. Not. R. Astron. Soc. **521**, 1393 (2023)
48. N. Sennett, T. Hinderer, J. Steinhoff, A. Buonanno, S. Ossokine, Phys. Rev. D **96**, 024002 (2017)
49. J. Ovalle, R. Casadio, R. da Rocha, A. Sotomayor, Eur. Phys. J. C **78**, 122 (2018)
50. J. Ovalle, A. Sotomayor, Eur. Phys. J. Plus **133**(10), 428 (2018). https://doi.org/10.1140/epjp/i2018-12291-7
51. L. Gabbanelli, J. Ovalle, A. Sotomayor, Z. Stuchlik, R. Casadio, Eur. Phys. J. C **79**(6), 486 (2019)
52. R. Casadio, E. Contreras, J. Ovalle, A. Sotomayor, Z. Stuchlick, Eur. Phys. J. C **79**(10), 826 (2019)
53. J. Ovalle, C. Posada, Z. Stuchlík, Class. Quantum Gravity **36**(20), 205010 (2019)
54. M. Sharif, A. Majid, Phys. Dark Universe **30**, 100610 (2020)
55. E. Contreras, F. Tello-Ortiz, S.K. Maurya, Class. Quantum Gravity **37**, 155002 (2020)
56. G. Abellan, A. Rincon, E. Fuenmayor, E. Contreras, Eur. Phys. J. Plus **135**, 606 (2020)
57. A. Rincon, L. Gabbanelli, E. Contreras, F. Tello-Ortiz, Eur. Phys. J. C **79**, 873 (2019)
58. A. Rincon, E. Contreras, F. Tello-Ortiz, P. Bargueno, G. Abellán, Eur. Phys. J. C **80**, 490 (2020)
59. M. Zubair, H. Azmat, Ann. Phys. **420**, 168248 (2020)
60. R. Casadio, J. Ovalle, R.A. da Rocha, Class. Quantum Gravity **32**, 215020 (2015)
61. E. Contreras, P. Bargueno, Eur. Phys. J. C **78**, 558 (2018)
62. E. Contreras, P. Bargueno, Class. Quantum Gravity **36**, 215009 (2019)
63. M.A. Ruderman, Annu. Rev. Astron. Astrophys. **10**, 427 (1972)
64. V. Canuto, Annu. Rev. Astron. Astrophys. **12**, 167 (1974)
65. R.L. Bowers, E.P.T. Liang, ApJ **188**, 657 (1974)
66. L. Herrera, N.O. Santos, Phys. Rep. **286**, 53 (1997)
67. R. Sawyer, D. Scalapino, PhRvD **7**, 953 (1973)
68. R. Sawyer, A. Soni, ApJ **216**, 73 (1977)
69. J. Martinez, PhRvD **53**, 6921 (1996)
70. L. Herrera, N.O. Santos, PhRp **286**, 53 (1997)
71. S. Chandrasekhar, PhRvL **12**, 114 (1964)
72. L. Herrera, Phys. Rev. D **101**, 104024 (2020)
73. J.M.Z. Pretel, Eur. Phys. J. C **80**, 726 (2020)
74. K. Chatziioannou, Gen. Relativ. Gravit. **52**, 109 (2020)
75. A. Bauswein, O. Just, H.-T. Janka, N. Stergioulas, Astrophys. J. **850**, L34 (2017)
76. F.J. Fattoyev, J. Piekarewicz, C.J. Horowitz, Phys. Rev. Lett. **120**, 172702 (2018)
77. B.P. Abbott et al., Virgo, LIGO Scientific, Phys. Rev. Lett. **121**, 161101 (2018)
78. E. Annala, T. Gorda, A. Kurkela, A. Vuorinen, Phys. Rev. Lett. **120**, 172703 (2018)
79. E.R. Most, L.R. Weih, L. Rezzolla, J. Schaffner-Bielich, Phys. Rev. Lett. **120**, 261103 (2018)
80. I. Tews, J. Margueron, S. Reddy, Phys. Rev. C **98**, 045804 (2018)
81. T. Malik, N. Alam, M. Fortin, C. Providencia, B.K. Agrawal, T.K. Jha, B. Kumar, S.K. Patra, Phys. Rev. C **98**, 035804 (2018)
82. D. Radice, A. Perego, F. Zappa, S. Bernuzzi, Astrophys. J. Lett. **852**, L29 (2018)
83. I. Tews, J. Margueron, S. Reddy, Eur. Phys. J. A **55**, 97 (2019)
84. C.D. Capano et al., Nat. Astron. **4**, 625 (2019)
85. R. Abbott et al. (LIGO Scientific and Virgo), Astrophys. J. Lett. **896**(2), L44 (2020)
86. R. Abbott et al. (KAGRA, VIRGO and LIGO Scientific), Phys. Rev. X **13**(4), 041039 (2023)
87. C.D. Bailyn, R.K. Jain, P. Coppi, J.A. Orosz, Astrophys. J. **499**, 367 (1998)
88. S.K. Maurya, M. Govender, G. Mustafa, R. Nag, EPJC **82**, 1006 (2022)
89. S.K. Maurya, K.N. Singh, M. Govender, S. Ray, Forts **71**, 2300023 (2023)
90. S.K. Maurya, A. Errehymy, M. Govender, G. Mustafa, N. Al-Harbi, A.H. Abdel-Aty, EPJC **83**, 348 (2023)
91. S. Maurya, G. Mustafa, S. Ray, B. Dayanandan, A. Aziz, A. Errehymy, Phys. Dark Universe **42**, 101284 (2023)
92. Herrera, Phys. Rev. D **97**, 044010 (2018)
93. M.C. Durgapal, R.S. Fuloria, Gen. Relativ. Gravit. **17**, 671 (1985)
94. Contreras, Stuchlik, Eur. Phys. J. C **82**, 706 (2022)
95. S.K. Maurya, K.N. Singh, A. Aziz, S. Ray, G. Mustafa, MNRAS **527**, 5192 (2024)
96. K.G. Begeman, A.H. Broeils, R.H. Sanders, MNRAS **249**, 523 (1991)
97. R. Jimenez, L. Verde, S.P. Oh, MNRAS **339**, 243 (2003)
98. Y.N. Vlasenko, P.I. Pronin, Moscow Univ. Phys. Bull. **39**, 89 (1984)
99. P. Demorest, T. Pennucci, S. Ransom, M. Roberts, J. Hessels, Nature **467**, 1081–1083 (2010)
100. R.W. Romani, D. Kandel, A.V. Filippenko, T.G. Brink, W. Zheng, Astrophys. J. Lett. **934**(2), L17 (2022)
101. M. Fortin, J.L. Zdunik, P. Haensel, M. Bejger, A&A **576**, A68 (2015)
102. F. Özel, P. Freire, ARA&A **54**, 401 (2016)
103. M.C. Miller, F.K. Lamb, A.J. Dittmann et al., ApJ **887**, L24 (2019)
104. T.E. Riley, A.L. Watts, P.S. Ray et al., ApJL **918**, L27 (2021)
105. M.C. Miller, F.K. Lamb, A.J. Dittmann et al., ApJL **918**, L28 (2021)
106. B.P. Abbott, R. Abbott, T.D. Abbott et al., PhRvL **121**, 161101 (2018)
107. J.M. Lattimer, B.F. Schutz, Astrophys. J. **629**, 979–984 (2005)

108. M. Kramer, N. Wex, Class. Quantum Gravity **26**, 073001 (2009)
109. M. Bejger, P. Haensel, Astron. Astrophys. **396**, 917 (2002)
110. A. Ray, B. Datta, Astrophys. J. **282**, 542–549 (1984)
111. P. Haensel, The magnetospheric structure and emission mechanisms of radio pulsars, in ed. by T.H. Hankins, J.M. Rankin, J. Gil (Pedagogical University Press, Zielona Góra), IAU Colloquium No. 128, 127 (1990)
112. L. Herrera, Phys. Lett. A **165**, 206 (1992)
113. H. Heintzmann, W. Heintzmann, A&A **38**, 51 (1975)
114. H. Bondi, MNRAS **259**, 365 (1992)
115. R. Chan, L. Herrera, N.O. Santos, CQGra **9**, 133 (1992)
116. R. Chan, L. Herrera, N.O. Santos, MNRAS **265**, 533 (1993)
117. R.C. Tolman, Phys. Rev. **55**, 364 (1939)
118. J.R. Oppenheimer, G.M. Volkoff, Phys. Rev. **55**, 374 (1939)
119. M.K. Gokhroo, A.L. Mehra, Gen. Relativ. Gravit. **26**, 75 (1994)
120. M.K. Mak, T. Harko, Chin. J. Astron. Astrophys. **2**, 248 (2002)
121. J. Ovalle, Phys. Rev. D **95**, 104019 (2017)
122. S.K. Maurya, K.N. Singh, M. Govender, G. Mustafa, S. Ray, Astrophys. J. Suppl. **269**(2), 35 (2023)
123. S.K. Maurya, G. Mustafa, M. Govender, K. Newton Singh, JCAP **10**, 003 (2022)
124. K.G. Begeman, A.H. Broeils, R.H. Sanders, Mon. Not. R. Astron. Soc. **249**, 523 (1991)
125. R. Jimenez, L. Verde, S.P. Oh, Mon. Not. R. Astron. Soc. **339**, 243 (2003)